Hans-Jürgen Butt, Doris Vollmer and Periklis Papadopoulos
Adv. Colloid Interface Sci. (2015), 222, pp 104–109

Super liquid-repellent layers: The smaller the better

Hans-Jürgen Butt, Doris Vollmer, Periklis Papadopoulos

Max Planck Institute for Polymer Research, Ackermannweg 10, D-55128 Mainz, Germany

butt@mpip-mainz.mpg.de

Super liquid-repellent layers need to have a high impalement pressure and high contact angles, in particular a high apparent receding contact angle. Here, we demonstrate that to achieve both, the features constituting the layer should be as small as possible. Therefore, two models for super liquid-repellent layers are theoretically analyzed: A superhydrophobic layer consisting of an array of cylindrical micropillars and a superamphiphobic layer of an array of pillars of spheres. For the cylindrical micropillars a simple expression for the apparent receding contact angle is derived. It is based on a force balance rather than a thermodynamic approach. The model is supported by confocal microscope images of a water drop on an array of hydrophobic cylindrical pillars. The ratio of the width of a pillar w to the center-to-center spacing a is a primary factor in controlling the receding angle. Keeping the ratio w/a constant, the absolute size of surface features should be as small as possible, to maximize the impalement pressure.

Keywords: Cassie state, Superhydrophobicity, Superamphiphobicity, Superoleophobicity, Wenzel state, Wetting

Highlights:

- Superhydrophobic and superoleophobic structures should be as small as possible
- Scaling down superamphiphobic surfaces leads to a high impalement pressure and a high contact angle

- The apparent receding contact angle is related to the capillary force of individual pillars

1. Introduction

Super liquid-repellent surfaces show a high apparent contact angle with a liquid, $\Theta^{app} \geq 150°$, and a low roll-off angle for drops. In the last years the interest in super liquid-repellency has grown enormously since it may open new opportunities both for research and technology. These include self-cleaning, drag reduction [1-4], fog harvesting [5], enhanced heat transfer [6], and gas exchange [2, 7]. In microfluidics tiny amounts of liquids can be manipulated with little adhesion and thus little energy dissipation.

To achieve high apparent contact angles the surfaces have to be structured on the nano- and micrometer length scale. This structure needs to be such that protrusions keep the drop from direct contact with the substrate by capillary forces. A layer of air needs to be maintained underneath a drop over a large part of the apparent contact area, leading to the so-called Cassie or Fakir state. In contrast, when the liquid infuses the surface structure without trapping air we talk about the Wenzel state. In the Wenzel state, super liquid-repellency is not achieved. In addition to the topology also one material property is important for the entrapment of air: The material's contact angle. It is determined by to the surface tensions of the liquid, γ_L, the surface tension of the solid, γ_S, and the solid/liquid interfacial tension, γ_{SL}. The material's contact angle, also called microscopic contact angle Θ, is formed on perfectly planar, smooth surfaces. It is given by Young's equation:

$$\gamma_L \cos\Theta = \gamma_S - \gamma_{SL} \quad (1)$$

A necessary condition for maintaining a layer of air underneath a drop is that the surface structures exceed a slope ψ of 180°-Θ (Fig. 1) [8]. Then at zero applied pressure the liquid can form a stable structure with air underneath.

For water as a liquid the entrapment of air is relatively easy to achieve. Many materials such as aliphatic hydrocarbons and perfluoroalkanes form a materials contact angle Θ above 90° with water. Therefore, micropillars with vertical walls are sufficient to build a superhydrophobic layer. For non-polar liquids overhanging structures are required [8-12] since Θ is below 90°.

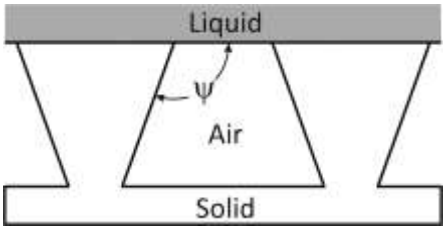

Figure 1: Schematic of a solid surface with a structure entrapping air underneath a liquid drop when the slope with the horizontal ψ exceeds 180°-Θ.

On nano- or microstructured surfaces the contact angle depends on the length scale one is looking at. Correspondingly, it is necessary to distinguish the material's contact angles from the apparent (macroscopic) contact angles. The material's contact angle, introduced above is the contact angle formed by the liquid when extrapolating the liquid shape on the 10 – 1000 nm scale to the contact line. We avoid the 10 nm close to the contact line because interfacial forces between the solid-liquid and liquid/air interface can lead to a change in the shape of the liquid surface [13-15]. The macroscopic scale is the length scale observed by eye or with a low-resolution microscope. It is larger than the nano- and microstructures forming the super liquid-repellent layer, thus typically larger than 10 µm. We call the macroscopic contact angle also apparent contact angle. We also distinguish between the *three phase contact line* (or simply contact line) on the microscopic and the *edge* on the macroscopic length scale [16].

A fundamental task is to link the material's and apparent contact angles. The contact angle for superhydrophobic surfaces is often calculated with the Cassie-Baxter-equation [17]:

$$\cos\Theta^{app} = \phi\left(\cos\Theta + 1\right) - 1 \qquad (2)$$

Here, ϕ is the area fraction of solid/liquid interface to the total projected surface area. For example, for a sessile water drop on top of a square array of cylindrical, hydrophobic pillars with radius R and spacing a the area fraction is $\phi = \pi R^2/a^2$ (Fig. 2). Θ^{app} is an average between the materials contact angle on the solid surface and the angle with air (180°) weighted by their respective proportions. Eq. (2) shows that one should expect the same contact angle for equal ratios of R/a. Inserting $\phi = \pi R^2/a^2$ and rearranging for R leads to

$$R = \frac{a}{\sqrt{\pi}}\sqrt{\frac{\cos\Theta^{app} + 1}{\cos\Theta + 1}} \qquad (3)$$

For a given material's contact angle Θ and a desired apparent contact angle Θ^{app} the pillar radius increases linearly with the pillar spacing.

The Cassie-Baxter equation is derived assuming thermodynamic equilibrium. However, liquid drops are often *not* in global thermodynamic equilibrium and their shape is determined by pinning of the edge [8, 18-26]. They are in a metastable state and not in a global energy minimum. Therefore, on real surfaces the contact angle for an advancing liquid front is larger than the one for a receding liquid. We distinguish between advancing Θ_a and receding material's contact angles Θ_r. On the macroscopic length scale we discriminate between *apparent* advancing and *apparent* receding contact angles, denoted by Θ_a^{app} and Θ_r^{app}, respectively. Θ_r^{app} is also called depinning contact angle.

Since liquid drops are usually not in thermodynamic equilibrium, in particular not on micro-structured surfaces, Eq. (2) is not applicable to calculate Θ_r^{app} or Θ_a^{app} for super liquid-repellent layers. Choi et al. introduced a differential parameter to extend the applicability of the Cassie-Baxter equation [22]. Mognetti and Yeomans [24] simulated receding apparent contact angles for regular arrays of micropillars with a Ginzburg-Landau free energy model. They confirm that the local pillar concentration is the primary factor determining Θ_r^{app}. Using a force balance between the weight of a liquid drop and surface tensional forces Extrand derived an apparent receding contact angle for a drop in the Cassie state as [8]

$$\Theta_r^{app} = \lambda_p \Theta_r + \left(1-\lambda_p\right)180° \qquad (4)$$

Here, λ_p is the linear fraction of the edge on the asperities. As the linear fraction is proportional to R/a, the same apparent contact angle is again expected for the same R/a ratio.[27] Extrand also concluded that to achieve a high impalement pressure and low contact angle hysteresis for water on micropillar surfaces asperity size and spacing should be small [27].

2. Objective and model

Here we demonstrate that to create a robust Cassie state, super liquid-repellent layers should be made of small structures. Only then a high impalement pressure *and* a high apparent receding contact angle can be achieved at the same time. We focus on the receding apparent contact angle Θ_r^{app} because it is more important than the advancing apparent contact angle Θ_a^{app}. For example, a high Θ_r^{app} guarantees a low roll-off angle [28, 29]. Therefore we systematically analyze the wetting of two representative models (Fig. 2):

- Water on a superhydrophobic array of cylindrical micropillars of radius R with flat top faces arranged in a square lattice of lattice constant a. For simplicity we assume that the pillars are relatively high so that sagging does not lead to contact between the liquid and

the bottom substrate. The materials advancing contact angle of water with the surface is $\Theta_a > 90°$; typically it is 100-120°.

- A non-polar liquid on a superamphiphobic square array of micropillars. Each pillar consists of a stack of spheres of radius R rigidly sintered together. The angle describing the neck β is supposed be small ($\beta \leq 30°$) to keep sufficient overhangs. The material's advancing contact angle is lower than 90°; typically it is Θ_a = 50-70°.

In both cases we assume a low surface energy material. The question is: How should one choose the available design parameters a and R to achieve a high impalement pressure and a high apparent receding contact angle?

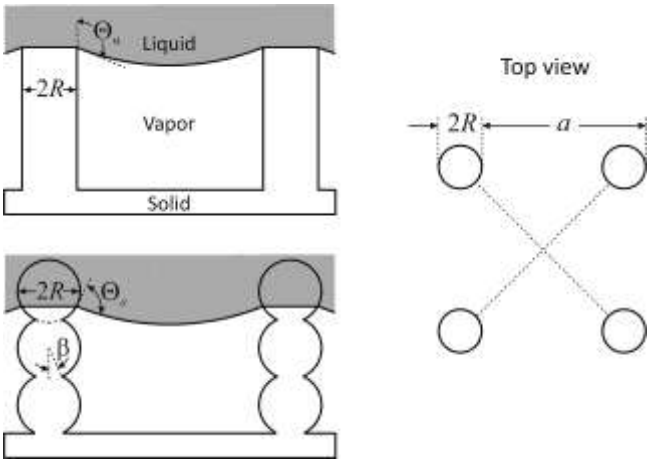

Figure 2. Schematic of square array of micropillars from side and top view. Top: Cylindrical pillars; bottom: pillars of sintered spheres. The liquid is suspended on top in the Cassie state.

3. Drop of water on a superhydrophobic layer

Impalement pressure

We consider the impalement pressure, that is the maximal pressure support before the liquid infuses the layer and the Wenzel state is reached. For cylindrical pillars the capillary force per pillar is equal to the periphery $2\pi R$ times the vertical component of the surface tension $-\gamma_L \cos\Theta_a$ [30-33]. Dividing this force by the area per pillar $A = a^2$ leads to an impalement pressure of

$$P^{\max}\left(1-\phi\right) = -\frac{2\pi R\gamma_L}{A}\cos\Theta_a \qquad (5)$$

with the area fraction $\phi = \pi R^2/A$. For an hexagonal array $A = a^2 \sin 60°$. The factor (1-ϕ) takes into account that the capillary force only needs to support the liquid above the free

surface [34]. Above solid/liquid interface the pressure is directly supported by the solid pillar surface. Since in most applications $\phi \leq 0.2$, the additional factor can usually be neglected. In Eq. (5) it was assumed that the microscopic contact angle around the contact line is the same in all directions. In reality, the microscopic contact angle in the direction towards the next pillar is slightly different from the microscopic contact angle in a direction along the diagonal of the square lattice [34, 35].

Although Eq. (5) is only a good approximation for $a >> R$, we still use it to illustrate the scaling of lines of constant impalement pressure (Fig. 3); for a justification see [16]. Solving Eq. (5) with respect to R leads to

$$R = \frac{\gamma_L}{P^{\max}} \cos\Theta_a + \sqrt{\left(\frac{\gamma_L}{P^{\max}} \cos\Theta_a\right)^2 + \frac{a^2}{\pi}} \qquad (6)$$

For one example, namely an advancing materials contact angle Θ_a = 120°, R is plotted versus a for a fixed P^{max} = 3 kPa (Fig. 3). In a double logarithmic plot Eq. (6) leads to straight line with a slope of two. At high spacing it levels off. In order to prevent impalement up to at least 3 kPa, the parameters R and a need to be chosen above this line. A second line with a slope 1 limits the radius of the cylinders for pure geometrical reasons to $a > 2R$. The grey area between those two lines indicates the allowed parameter range. When requiring a higher impalement pressure the graph R-vs-a for constant P^{max} shifts upwards and the "allowed" grey triangle decreases in size.

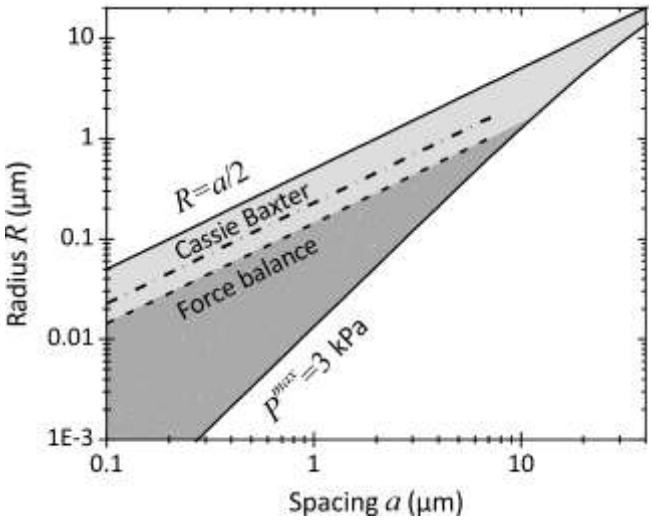

Figure 3. Radius of cylindrical pillars versus center-to-center spacing for an array of hydrophobic pillars, water (γ_L = 0.072 N/m), and a material's advancing contact angle of Θ_a = 120°. The line "R=a/2" indicates the geometrically possible limit. The steeper line "P^{max} =3 kPa"

indicates a minimum radius required for 3 kPa impalement pressure calculated with Eq. (6). In addition, lines for constant Θ_r^{app} = 150° were calculated with the Cassie-Baxter Eq. (3), Θ = 100°, dotted, and from the force balance Eq. (12), dashed, with Θ_r = 100°. The dark grey area indicates the parameter space for which $\Theta_r^{app} \geq 150°$ and $P^{\max} \geq 3$ kPa.

Microscopic structure of the liquid

To find an appropriate model linking Θ_r^{app} to Θ_r it is necessary to consider the microscopic structure of the liquid on an array of micropillars. Therefore, we imaged a slowly evaporating water drop on an array of cylindrical micropillars by laser scanning confocal microscopy (Fig. 4a,b). The procedure was similar to the one followed for the study of the Cassie-Wenzel transition [35]. The air cushion underneath the drop is clearly visible in the confocal images. Capillary bridges are formed between the top faces of the pillars and the drop. Such bridges have been observed before [22, 25, 35-37]. At the edge, these bridges form neck-like structures. The total curvature in theses liquid necks is low because the Laplace pressure of the liquid is determined by the macroscopic radius of the drop. The contact angle at the receding side of the pillar at the edge is about 85°, which is the receding material's contact angle of water. In addition, the length of the capillary bridge is nearly equal to the diameter of the pillar. Already 20 µm above the pillars the shape becomes a spherical cap and local variations due to the presence of isolated capillary bridges vanish. For a drop to recede or roll the bridges at the rear have to be broken. Since the energy of an individual bridge is orders of magnitude higher than the thermal energy k_BT, such drops are usually not in thermodynamic equilibrium but their specific shape depends on the history. The confocal images are the basis of the calculations of macroscopic contact angles below.

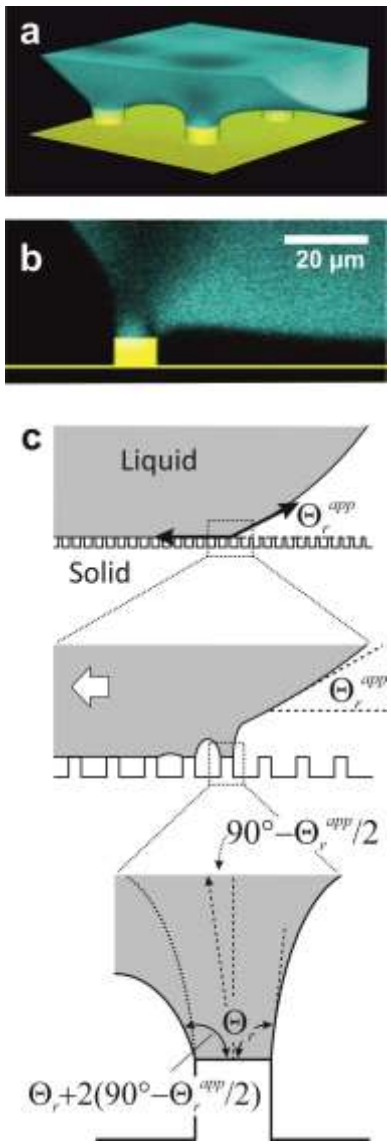

Figure 4. (a) Three-dimensional confocal microscope image of an initially 6 µL water drop on a square array of cylindrical SU-8 pillars (5 µm high, 10 µm diameter, center-to-center distance 40 µm). SU-8 was labeled with *N*-(2,6-diisopropylphenyl)-3,4-perylenedicarboxylic acid monoimide (PMI), emission maximum at 540 nm. The array was hydrophobized with 1*H*,1*H*,2*H*,2*H*-perfluorooctyl-trichlorosilane by chemical vapor deposition. Water was labeled with the water-soluble dye *N*,*N*'-(2,6-diisopropylphenyl)-1,6,7,12-tetra(1-methylpyridinium-3-yloxy)-perylene-3,4,9,10-tetracarboxylic acid diimide tetramethane-sulfonate (WS-PDI), emission at 590 nm. Measurements of the surface tension with the Wilhelmy plate method (platinum plate, DCAT11 tensiometer, DataPhysics Instruments GmbH) verified that the dye had no effect on the surface tension at 0.1 mg/mL concentration. Confocal microscopy was performed with a Leica TCS SP5 microscope with a resonant scanner at 8 kHz, allowing for

the acquisition of a complete 3D stack (86×86×35 μm^3) within 4.8 s. To obtain the correct coordinates for the water-air interface a dry objective 40×/0.85 was used. This had the side effect that pillars appeared shorter by a factor equal to the refractive index n_{SU8} = 1.6. Therefore, they were replaced by yellow „artificial“ pillars in Fig. 4. (b) Two-dimensional vertical (xz) cross-section along the diagonal. (c) Schematic of the rear edge of a drop on an array of micropillars. The actual capillary bridge can be approximated by a rotationally symmetric bridge rotated by $90° - \Theta_r^{app}/2$.

Calculation of apparent receding contact angle

To link the apparent contact angle to the microscopic surface structure and the materials contact angle we explicitly consider the force of individual liquid necks and apply a force balance. The fact that a drop is not in a global free energy minimum is considered on two length scales. First on the nanometer scale by discriminating between advancing and receding materials contact angle. On the larger scale, capillary bridges form between a receding drop and the top faces of micropillars. These bridges are stable but they do not represent a global energy minimum. We proceed in two steps. First we calculate the maximal force a rotationally symmetric capillary bridge can hold. Second, we consider the effect when tilting the bridge. We equate the horizontal force component of such a bridge to the macroscopic horizontal force component.

The maximal capillary force a rotationally symmetric liquid meniscus can hold in normal direction is the integral of the normal component of the surface tension around the contact line. The liquid bridge collapses when the actual microscopic contact angle decreases below the receding contact angle; this condition is referred to as the Gibbs criterion [24]. Therefore, just before the capillary bridge collapses the force of a single liquid meniscus is $f = 2\pi R\gamma_L \sin\Theta_r$ for $\Theta_r \geq 90°$ and $f = 2\pi R\gamma_L$ for $\Theta_r < 90°$. This is not 100% correct since we ignore the Laplace pressure. It is, however a good approximation. The force due the Laplace pressure acting on an the top face of a pillar can be calculated from $f = 2\gamma_L \pi R^2/r_d$, where r_d is the radius of curvature of the drop. Since $R/r_d \ll 1$ we neglect it. See [38] for a correction calculated with the full Laplace equation. We take deviations with a correction factor α into account:

$$f = \alpha 2\pi R\gamma_L \sin\Theta_r \qquad (7)$$

α is of the order of 1 and depends on the specific geometry of the contact.

At edge of the drop the capillary force of the meniscus is not directed normal to the surface but in a direction 90°-$\Theta_r^{app}/2$ with respect to the normal (Fig. 4c). The horizontal component is obtained by multiplying f with $\sin\left(\pi/2-\Theta_r^{app}/2\right)=\cos\left(\Theta_r^{app}/2\right)$. Just before the liquid recedes macroscopically this horizontal component is balanced by the surface tensional force per unit length of the edge $\gamma_L\left(1+\cos\Theta_r^{app}\right)$ [16] (Fig. 4c). If we equate both for a line parallel to the rows of pillars we get a force per unit length of the rim of

$$\gamma_L\frac{2\pi\alpha R}{a}\sin\Theta_r\cos\frac{\Theta_r^{app}}{2}=\gamma_L\left(1+\cos\Theta_r^{app}\right)\Rightarrow\frac{2\pi\alpha R}{a}\sin\Theta_r=\frac{1+\cos\Theta_r^{app}}{\cos\dfrac{\Theta_r^{app}}{2}} \tag{8}$$

Using the mathematical identity $\left(1+\cos x\right)/\cos\left(x/2\right)=2\cos\left(x/2\right)$ it follows that

$$\frac{\pi\alpha R}{a}\sin\Theta_r=\cos\frac{\Theta_r^{app}}{2} \tag{9}$$

Tilting the capillary bridge also has a second effect: The force f becomes weaker. Rather than having an adhesion force $f=2\pi R\gamma_L\sin\Theta_r$ one would need to solve the integral of the normal force around the circumference: $f=\gamma_L R\int_0^{2\pi}\sin\Theta(\vartheta)d\vartheta$, where ϑ is the angle around the contact line on top of a pillar. Just before the drop starts to recede at the outer rim the actual contact angle is Θ_r. At the inner side the contact angle at that point is still larger:

$$\Theta=\Theta_r+2\left(90°-\frac{\Theta_r^{app}}{2}\right) \tag{10}$$

For simplicity we assume that the actual microscopic contact angle smoothly changes around the periphery with the azimuthal angle ϑ. Therefore, as an average the contact angle is $\bar{\Theta}\approx\Theta_r+\left(90°-\Theta_r^{app}/2\right)$. Inserting this corrected microscopic contact angle into Eq. (9) leads to

$$\frac{\pi\alpha R}{a}\cos\left(\Theta_r-\frac{\Theta_r^{app}}{2}\right)=\frac{\pi\alpha R}{a}\left(\cos\Theta_r\cos\frac{\Theta_r^{app}}{2}+\sin\Theta_r\sin\frac{\Theta_r^{app}}{2}\right)=\cos\frac{\Theta_r^{app}}{2} \tag{11}$$

Further rearranging:

$$\tan\frac{\Theta_r^{app}}{2}=\frac{a}{\pi\alpha R\sin\Theta_r}-\frac{1}{\tan\Theta_r} \tag{12}$$

or

$$\Theta_r^{app} = 2\arctan\left(\frac{a}{\pi\alpha R\sin\Theta_r} - \frac{1}{\tan\Theta_r}\right) \quad (13)$$

As in the Cassie-Baxter equation the apparent contact angle depends on the ratio of a/R. If we do the same calculation for square pillars we need to replace $2\pi R$ in Eq. (7) by the periphery $4b$, where b is the length of one side. This leads to

$$\Theta_r^{app} = 2\arctan\left(\frac{a}{\alpha 2b\sin\Theta_r} - \frac{1}{\tan\Theta_r}\right) \quad (14)$$

Lines of constant Θ_r^{app} calculated with Eq. (12) are plotted in Figure 3 indicated by "force balance". Here, the parameter α was chosen to be $\alpha = 2/\pi$ so that $f = 4R\gamma_L \sin\Theta_r$; the capillary force is takeover a length twice the width of the pillar. The radius R required to achieve Θ_r^{app} = 150° increases linearly with the spacing. For higher apparent contact angle this line would move downwards. For comparison also R-vs-a calculated with the Cassie-Baxter Eq. (3) is plotted for an apparent contact angle of 150°. The radii are typically 1.6 times higher than the ones calculated with Eq. (12).

Figure 5 shows apparent receding contact angles reported in the literature for arrays of cylindrical [39] and square pillars [18] versus the ratio of width to pitch w/a. The width is $2R$ for cylindrical pillars and b for square pillars. Best fits were obtained with α = 0.65 for cylindrical pillars and α = 0.46 for square pillars. Results reported by Bico et al. [40] and Moulinet and Bartolo [41] for arrays of cylindrical pillars agreed with calculated values for α = 0.59 and α = 0.56, respectively. The Cassie-Baxter equation (4) tends to overestimate receding apparent contact angles. The force balance leading to Eqs. (13) and (14) led to good agreement when choosing α = 0.6 for cylindrical pillars and α = 0.46 for square pillars. Realizing that $0.6\pi R = 1.9R \approx 2R$ and $0.46\cdot 2b \approx b$ we can generalize Eqs. (13) and (14):

$$\Theta_r^{app} \approx 2\arctan\left(\frac{a}{w\sin\Theta_r} - \frac{1}{\tan\Theta_r}\right) \quad (15)$$

Here, $w = 2R$ for cylindrical pillars and $w = b$ for square pillars.

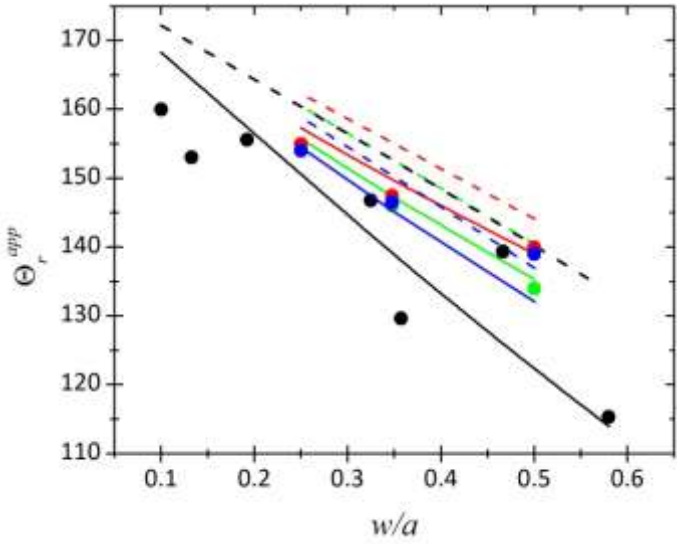

Figure 5. Comparison of apparent receding contact angles calculated with measured values for arrays of cylindrical and square pillars. Θ_r^{app} is plotted versus the ratio of width to center-to-center distance. The width is $w=2R$ for cylindrical pillars and $w=b$ for square pillars. Experimental results were taken from Callies et al. [39] (black circle, square array of cylindrical silicon pillars with Θ_r = 80°), Öner & MacCarthy [18] (hexagonal array of silicon square pillars hydrophobized using *n*-octyldimethylchlorosilane Θ_r = 94° blue circle, dimethyldichlorosilane Θ_r = 102° green circles, and $CF_3(CF_2)14(CH_2)_2$-$(CH_3)_2SiCl$ Θ_r = 110° red circles). Θ_r^{app} values calculated with Eq. (13) and α=0.65 are plotted as a continuous black line. Dashed black lines are predictions with the Cassie-Baxter Eq. (2). For square pillars experimental results are compared to values calculated with Eq. (13, continuous in corresponding color) for α = 0.46 and to the Eq. (2, dashed).

Using Eq. (13) we can add lines of constant receding contact angle into Figure 3. The force balance Eq. (13) leads to 1.6 times smaller cylinder radius than the one calculated with the Cassie-Baxter equation (4). If an apparent receding contact angle above 150° is required, only R values below this line are allowed. Thus, for $P_{max} \geq 3$ kPa and $\Theta_r^{app} \geq 150°$ only the dark grey triangle is allowed as a parameter range for R and a.

4. Drop of non-polar liquid on a superamphiphobic layer

In ref. [16] an equation was derived for the impalement pressure for $\phi \to 0$. Here, we consider the fact that the pressure in the area covered by pillars does not need to be balanced by a capillary forces. As in Eq. (2) this consideration led to an additional factor $1-\phi$, which was neglected in Eq. (6) of ref. [16]. The impalement pressure for a square array of pillars of spheres is given by

$$P^{\max}\left(1-\phi\right)=\frac{2\pi\gamma R}{a^2}\sin^2\frac{\Theta_a}{2} \tag{16}$$

With $\phi=\pi R^2/a^2$ we obtain in analogy to Eq. (6)

$$R=-\frac{\gamma}{P^{\max}}\sin^2\frac{\Theta_a}{2}\pm\sqrt{\left(\frac{\gamma}{P^{\max}}\sin^2\frac{\Theta_a}{2}\right)^2+\frac{a^2}{\pi}} \tag{17}$$

The corresponding plots of R-vs-a for P^{max} = 3 kPa are shown in figure 6. The light grey area shows possible parameters R and a for which the impalement pressure exceeds 3 kPa.

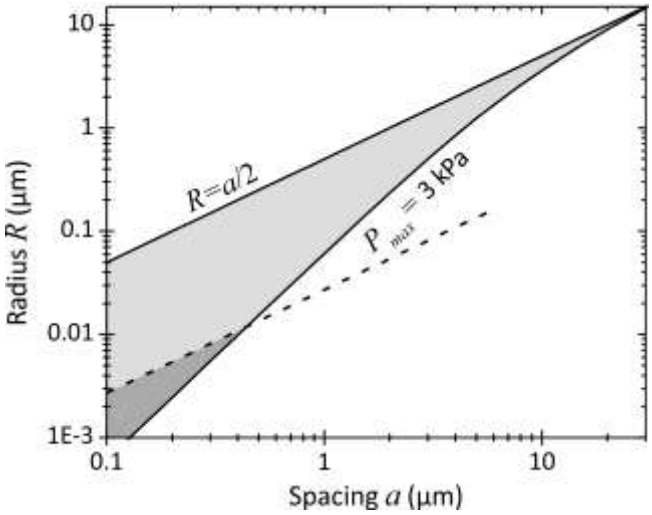

Figure 6. Radius of spheres versus center-to-center spacing for an array of hydrophobic pillars consisting of spheres for *n*-hexadecane (γ_L = 0.027 N/m) and a materials receding contact angle of Θ_r = 65°. The top line represents the geometric limit R=a/2. The steep line is an isobar for an impalement pressure of P_{max} = 3 kPa (Eq. 17). The dashed line is R-vs-a for a constant apparent contact angle Θ_r^{app} = 150° calculated with Eq. (18). The dark grey area indicates the parameter space for which $\Theta_r^{app}\geq 150°$ and $P^{\max}\geq 3$ kPa.

In addition to the lines of constant implement pressure we calculated lines for constant receding contact angle using [16]

$$\Theta_r^{app}=2\cdot\arccos\left(\frac{\pi R}{a}\cos^2\frac{\Theta_r}{2}\right)\Rightarrow R=\frac{a}{\pi}\left[\frac{\cos\left(\Theta_r^{app}/2\right)}{\cos\left(\Theta_r/2\right)}\right]^2 \tag{18}$$

The region in which $\Theta_r^{app}\geq 150°$ and $P^{max}\geq 3$ kPa is indicated in dark grey in figure 6. Figure 6 demonstrates that for a high impalement pressure *and* a high apparent receding contact angle the structures should be as small as possible.

5. Conclusion

Super liquid-repellent structures should be as small as possible. Scaling down the geometry of a super liquid-repellent structure allows for a high impalement pressure without affecting the high apparent contact angle. The simple continuum theory will at some nanoscale not be valid anymore. Therefore, in order to design super liquid-repellent surfaces on the nanoscale simulations will be necessary.

6. Acknowledgements

HJB wishes to thank the ERC for the advanced grant 340391-SUPRO. We acknowledge fruitful discussions with Kostas Daoulas, Burkhard Dünweg and Nikita Tretyakov.

7. References

[1] Watanabe K, Udagawa Y, Udagawa H. J. Fluid Mech. 1999; 381:225.

[2] McHale G, Newton MI, Shirtcliffe NJ. Soft Matter 2010; 6:714.

[3] Rothstein JP. Annu. Rev. Fluid Mech. 2010; 42:89.

[4] Busse A, Sandham ND, McHale G, Newton MI. J. Fluid Mech. 2013; 727:488.

[5] Park KC, Chhatre SS, Srinivasan S, Cohen RE, McKinley GH. Langmuir 2013; 29:13269.

[6] Miljkovic N, Wang EN. MRS Bulletin 2013; 38:397.

[7] Paven M, Papadopoulos P, Schöttler S, Deng X, Mailänder V, Vollmer D, Butt H-J. Nature Commun. 2013; 4:2512.

[8] Extrand CW. Langmuir 2002; 18:7991.

[9] Herminghaus S. Europhys. Lett. 2000; 52:165.

[10] Tuteja A, Choi W, Ma ML *et al.* Science 2007; 318:1618.

[11] Nosonovsky M. Langmuir 2007; 23:3157.

[12] Tuteja A, Choi WJ, McKinley GH, Cohen RE, Rubner MF. Mrs Bulletin 2008; 33:752.

[13] Zheleznyi BV. Dokl. Akad. Nauk SSSR 1972; 206:377.

[14] Wayner PC. J. Colloid Interface Sci. 1982; 88:294.

[15] Churaev NV, Starov VM, Derjaguin BV. J. Colloid Interface Sci. 1982; 89:16.

[16] Butt HJ, Semprebon C, Papadopoulos P, Vollmer D, Brinkmann M, Ciccotti M. Soft Matter 2013; 9:418.

[17] Cassie ABD, Baxter S. Trans. Faraday Soc. 1944; 40:546.

[18] Öner D, McCarthy TJ. Langmuir 2000; 16:7777.

[19] Yoshimitsu Z, Nakajima A, Watanabe T, Hashimoto K. Langmuir 2002; 18:5818.

[20] Dorrer C, Rühe J. Langmuir 2006; 22:7652.

[21] Gao L, McCarthy TJ. Langmuir 2007; 23:3762.

[22] Choi W, Tuteja A, Mabry JM, Cohen RE, McKinley GH. J. Colloid Interface Sci. 2009; 339:208.

[23] Reyssat M, Quéré D. J. Phys. Chem. B 2009; 113:3906.

[24] Mognetti BM, Yeomans JM. Langmuir 2010; 26:18162.

[25] Paxson AT, Varanasi KK. Nature commun. 2013; 4:1492.

[26] Gauthier A, Rivetti M, Teisseire J, Barthel E. Langmuir 2014; 30:1544.

[27] Extrand CW. Langmuir 2006; 22:1711.

[28] Olsen DA, Joyner PA, Olson MD. J. Phys. Chem. 1962; 66:883.

[29] Butt H-J, Roismann I, Brinkmann M, Papadopoulos P, Vollmer D, Semprebon C. Curr. Op. Colloid Interfaces Sci. 2014: online.

[30] Dettre RH, Johnson RE. SCI Monograph 1967; 25:144.

[31] Youngblood JP, McCarthy TJ. Macromolecules 1999; 32:6800.

[32] Bormashenko E, Musin A, Whyman G, Zinigrad M. Langmuir 2012; 28:3460.

[33] Zheng QS, Yu Y, Zhao ZH. Langmuir 2005; 21:12207.

[34] Lobaton EJ, Salamon TR. J. Colloid Interface Sci. 2007; 314:184.

[35] Papadopoulos P, Mammen L, Deng X, Vollmer D, Butt HJ. Proc. Natl. Acad. Sci. USA 2013; 110:3254.

[36] Papadopoulos P, Deng X, Mammen L *et al.* Langmuir 2012; 28:8392.

[37] Dufour R, Brunet P, Harnois M, Boukherroub R, Thomy V, Senez V. Small 2012; 8:1229.

[38] Huh C, Mason SG. Colloid & Polymer Sci. 1975; 253:566.

[39] Callies M, Chen Y, Marty F, Pepin A, Quéré D. Microelectronic engineering 2005; 78-79:100.

[40] Bico J, Marzolin C, Quéré D. Europhys. Lett. 1999; 47:220.

[41] Moulinet S, Bartolo D. Eur. Phys. J. E 2007; 24:251.